



Experimental and numerical characterization of the water flow in spacer-filled channels of spiral-wound membranes



Szilard S. Bucs^{a,*}, Rodrigo Valladares Linares^a, Jeremy O. Marston^b, Andrea I. Radu^{c,d}, Johannes S. Vrouwenvelder^{a,c,e}, Cristian Picioreanu^c

^a Water Desalination and Reuse Center, Division of Biological and Environmental Science and Engineering, King Abdullah University of Science and Technology, Thuwal, 23955-6900, Saudi Arabia

^b Department of Chemical Engineering, Texas Tech University, Lubbock, TX, 79409, USA

^c Department of Biotechnology, Faculty of Applied Sciences, Delft University of Technology, Julianalaan 67, 2628, BC Delft, The Netherlands

^d Chair of Building Physics, Swiss Federal Institute of Technology Zürich (ETHZ), Stefano-Francini-Platz 5, 8093, Zürich, Switzerland

^e Wetsus, European Centre of Excellence of Sustainable Water Technology, Oostergoweg 9, 8911 MA, Leeuwarden, The Netherlands

ARTICLE INFO

Article history:

Received 10 June 2015

Received in revised form

3 September 2015

Accepted 20 September 2015

Available online 25 September 2015

Keywords:

Particle image velocimetry (PIV)

Computational fluid dynamics (CFD)

Spacer

Spiral-wound membrane module

Membrane filtration

ABSTRACT

Micro-scale flow distribution in spacer-filled flow channels of spiral-wound membrane modules was determined with a particle image velocimetry system (PIV), aiming to elucidate the flow behaviour in spacer-filled flow channels. Two-dimensional water velocity fields were measured in a flow cell (representing the feed spacer-filled flow channel of a spiral wound reverse osmosis membrane module without permeate production) at several planes throughout the channel height. At linear flow velocities (volumetric flow rate per cross-section of the flow channel considering the channel porosity, also described as crossflow velocities) used in practice (0.074 and $0.163 \text{ m}\cdot\text{s}^{-1}$) the recorded flow was laminar with only slight unsteadiness in the upper velocity limit. At higher linear flow velocity ($0.3 \text{ m}\cdot\text{s}^{-1}$) the flow was observed to be unsteady and with recirculation zones. Measurements made at different locations in the flow cell exhibited very similar flow patterns within all feed spacer mesh elements, thus revealing the same hydrodynamic conditions along the length of the flow channel. Three-dimensional (3-D) computational fluid dynamics simulations were performed using the same geometries and flow parameters as the experiments, based on steady laminar flow assumption. The numerical results were in good agreement (0.85 – 0.95 Bray–Curtis similarity) with the measured flow fields at linear velocities of 0.074 and $0.163 \text{ m}\cdot\text{s}^{-1}$, thus supporting the use of model-based studies in the optimization of feed spacer geometries and operational conditions of spiral wound membrane systems.

© 2015 Elsevier Ltd. All rights reserved.

1. Introduction

Membrane filtration processes for seawater desalination and wastewater reuse are becoming increasingly important. In a spiral-wound membrane module, most commonly used in these water treatment processes, the membrane sheets are rolled around an inner tube. To keep the membrane leaves apart a relatively thin

spacer net is inserted. The feed spacer promotes flow instabilities to enhance mass transfer and reduce concentration polarization (Fimbres-Weihs et al., 2006; Gao et al., 2013). However, aside from a beneficial impact, the feed spacer also contributes to pressure drop increase along the flow channel. Furthermore, a major drawback in membrane technology is fouling, i.e. accumulation of unwanted material on the membrane and spacer surface (Antony et al., 2011; Baker and Dudley, 1998; Flemming, 2002; Ridgway et al., 1983; Salvador Cob et al., 2012). Micro-sized particles, colloids, organic macromolecules can deposit and microbial cells can attach, grow and form biofilms on the membrane and spacer surfaces and decrease the filtration performance (Flemming, 1997; Tang et al., 2011; Yiantsios and Karabelas, 2003). Baker and Dudley (1998) reported that initial deposition of fouling occurred on the feed spacer filaments and on the membrane alongside the spacer and,

* Corresponding author. King Abdullah University of Science and Technology, KAUST, Water Desalination and Reuse Center, Al-Jazri Bldg, Thuwal, 23955-6900, Saudi Arabia.

E-mail addresses: Szilard.Bucs@kaust.edu.sa, S.S.Bucs@tudelft.nl (S.S. Bucs), Rodrigo.Valladares@kaust.edu.sa (R. Valladares Linares), Jeremy.Marston@ttu.edu (J.O. Marston), Radu@arch.ethz.ch (A.I. Radu), J.S.Vrouwenvelder@tudelft.nl, Johannes.Vrouwenvelder@kaust.edu.sa, Hans.Vrouwenvelder@wetsus.nl (J.S. Vrouwenvelder), C.Picioreanu@tudelft.nl (C. Picioreanu).

with time, intruded upon the remaining free membrane area.

It was shown that fouling accumulation can be controlled to some degree by suitable hydrodynamic conditions (Sablani et al., 2001). Moreover, the same amount of accumulated fouling material can have a different impact on performance, depending on the hydrodynamic conditions (Araújo et al., 2012; Bucs et al., 2014; Valladares Linares et al., 2014; Vrouwenvelder et al., 2011). Feed spacer geometry and operational conditions (e.g., flow velocity, transmembrane pressure, etc.) have a profound influence on the flow pattern and foulant deposition in spacer-filled channels (Radu et al., 2014; Vrouwenvelder et al., 2009). To design new spacers with the least pressure drop, minimal fouling propensity, and maximum mass transfer, it is therefore important to both be able to determine experimentally and to numerically calculate the hydrodynamics (i.e., velocity and pressure profiles, shear at the walls, etc.) in these flow channels.

The impact of different spacer geometries on the flow pattern is not easily measurable experimentally due to the inherently small length-scales involved. Alternatively, advances in numerical performance have led to computational fluid dynamics (CFD) techniques being the primary means to understand the fluid flow in spacer-filled channels. Some studies have simulated fluid flow and mass transfer in simplified two-dimensional setups (Schwinge et al., 2002; Radu et al., 2010). However, in recent years, three-dimensional (3-D) numerical models are becoming increasingly accessible, developed mainly with an emphasis on the effect of feed spacer on hydrodynamics and mass transfer in feed spacer channels (Koutsou et al., 2007, 2009; Saeed et al., 2012). Simplified cylindrical shapes have been used for representation of spacer filaments in most of the numerical studies. However, microscopic observations of the feed spacer revealed that the spacers used in commercially available spiral-wound membrane modules have more irregular geometry, with filaments varying in thickness (Fimbres-Weihs and Wiley, 2010; Picioreanu et al., 2009; Vrouwenvelder et al., 2010). Simulations by Picioreanu et al. (2009) showed that the feed channel pressure drop for a simplified spacer with cylindrical filaments is significantly different from more realistic spacer geometry with variations in filament thickness. The importance of realistic spacer geometries in numerical studies was also revealed by a recent experimental and numerical study on particle deposition in spacer channels at various feed spacer orientations (Radu et al., 2014).

In contrast with the abundance of numerical studies, only a few experimental investigations were carried out to directly visualize and characterize the flow patterns in feed spacer-filled channels. This may be partly due to the geometrical complexity and small dimensions of the flow channels (thereby the need for microscopic techniques), but also due to the high temporal resolution required (i.e., very fast flows require use of fast cameras).

Nuclear magnetic resonance (NMR) or magnetic resonance imaging (MRI) has been used to locally resolve (in 3-D) the velocity and shear stress distribution in tube reactors containing biofilms (Manz et al., 2003; Wagner et al., 2010). In spacer-filled channels with and without biofilm, NMR was used to visualize and measure two-dimensional velocity profiles (Vrouwenvelder et al., 2010). Formation of preferential flow patterns was observed as biofouling evolved in time. However, as a limitation of the method used, the flow cell was operated with 10 times lower linear flow velocity than normally used in practice, and the measured velocity had to be averaged over the flow channel height.

Doppler optical coherence tomography (DOCT) was also used to measure and visualize the local velocity profile in a spacer-filled channel (Gao et al., 2013). The DOCT could reveal the flow profile normal to the main flow direction at different sections along the flow channel. Furthermore, the development of eddies were

observed next to the spacer filaments.

Particle image velocimetry (PIV) was used to characterize the flow next to the membrane surface at different linear flow velocities by Gimmelshtein and Semiat (2005) and Willems et al. (2010). Gimmelshtein and Semiat (2005) found laminar flow at commonly used linear flow velocities ($0.06\text{--}0.17\text{ m}\cdot\text{s}^{-1}$), with (expectedly) increasing mixing intensity at higher linear flow velocities. The measured flow fields were in good agreement with the two-dimensional numerical simulations developed by the authors (Gimmelshtein and Semiat, 2005). Willems et al. (2010) used PIV techniques to achieve a quantitative description of the two-phase flow in spacer-filled channel. Although the temporal resolution was low, the study showed how the flow direction changed along the channel height and also evaluated the impact of bubbly flow on local velocity. PIV techniques were also applied to investigate the flow patterns in flow channels using modified saw-tooth spacer geometries (Liu et al., 2015). However, the flow channel thickness (4 mm) in these experiments was much higher than in reverse osmosis/nanofiltration systems applied in practice.

In summary, all of these experimental methods have some limitations in terms of the flow channel thicknesses used, the applied linear flow velocity, the spatial or temporal resolution. As such, the objectives of this study were: (i) to evaluate the micro-scale flow patterns in a feed spacer-filled channel under conditions representative for current practical applications (i.e., similar linear flow velocity and channel dimensions) using a PIV system, and (ii) to compare the measured flow fields with three-dimensional numerical simulations.

2. Materials and methods

2.1. Experimental

Micro-scale fluid flow patterns in spacer-filled channels were experimentally investigated by particle image velocimetry (PIV).

2.1.1. Flow cell

For PIV measurements, a fully transparent flow cell was constructed from two high quality glass slides (2.5 cm width and 7.5 cm length, VWR International, West Chester, PA) (Fig. 1). Commercially available non-woven Toray feed spacer with 31 mil (0.787 mm) thickness was inserted between the glass slides. The height of the flow cell was adjusted to fit the feed spacer thickness and to avoid bypass flow below or above the spacer, then the whole ensemble was glued with epoxy resin on the sides. Water connectors were fabricated from nylon tubing with 4 mm (for inlet) and 6 mm (for outlet) inner diameter (Fig. 1).

In order to keep the flow cell transparent, no membrane sheets were inserted into the flow channel and the flow cell was operated without permeate production. The impact of permeation on the cross flow velocity in our lab scale flow cell (7.5 cm long) is negligible since the permeate velocity typically in the order of $10\text{ }\mu\text{m}\cdot\text{s}^{-1}$ (Radu et al., 2010) is four orders of magnitude lower than the linear flow velocity of the feed water (in the order of $10\text{ cm}\cdot\text{s}^{-1}$). Even without permeation, the presence of a membrane sheet instead of glass wall would not visibly influence the flow pattern, because the average roughness of an RO membrane is in the order of 50 nm (Ishigami et al., 2012), three orders of magnitude lower than our depth of field for flow visualization in z direction.

To eliminate pulsations generated by pumps, hydrostatic pressure was used instead to drive the water flow through the flow cell. A 3 L reservoir was placed about 1 m above the flow cell and connected to the flow cell inlet. The flow rate was adjusted with a valve connected to the flow cell outlet. To maintain constant flow rate the water level was kept constant in the reservoir by

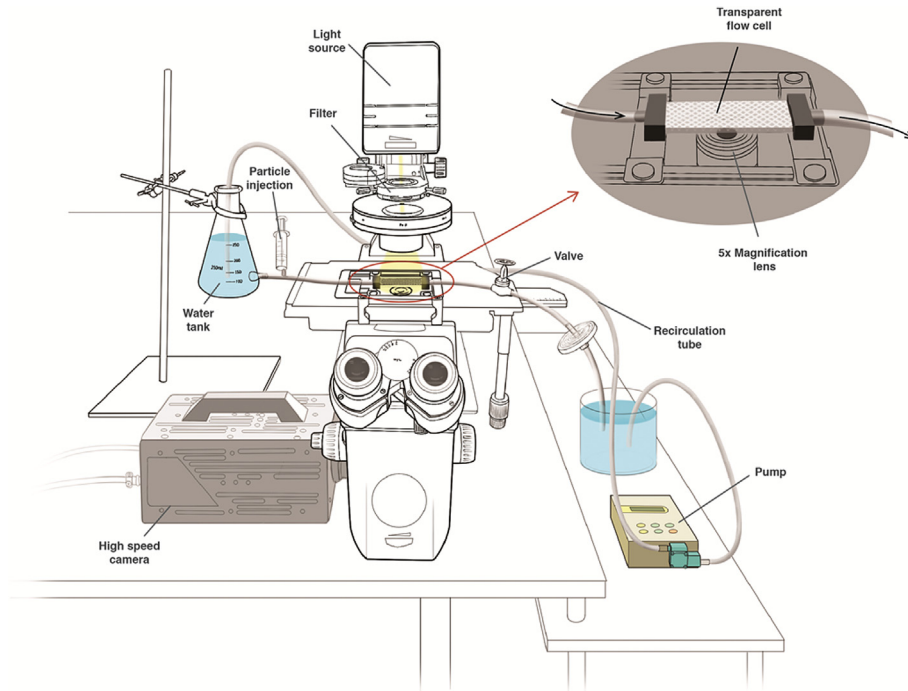


Fig. 1. Experimental setup used for water flow measurements and visualization, using particle image velocimetry (PIV). The experimental setup consisted of an elevated water tank, a transparent flow cell with a feed spacer, a particle injection point, a microscope and a high speed camera.

recirculating the water (Fig. 1). The Reynolds number was calculated according to Schock and Miquel (1987), Equation (1)

$$Re = \frac{u_m \cdot d_h \cdot \rho}{\eta} \quad (1)$$

with u_m being the imposed linear (i.e. average) flow velocity, ρ and η are the water density and viscosity at 20 °C (998 kg m⁻³ and 0.001 Pa s, respectively), and d_h is the hydraulic diameter (≈ 1 mm), calculated from the total volume between the glass slides, V_{Tot} , the spacer volume, V_{Sp} , and the wetted surface A_w including feed spacer and both glass slides (Schock and Miquel, 1987).

$$d_h = \frac{4(V_{Tot} - V_{Sp})}{A_w} \quad (2)$$

The flow rate was measured gravimetrically at the outlet. Measurements were performed at three linear inflow velocities: $u_m = 0.163$ m·s⁻¹ (Re = 160), 0.074 m·s⁻¹ (Re = 70) and 0.294 m·s⁻¹ (Re = 300).

2.1.2. Particles

For flow visualization, silver coated hollow glass beads of 10 μ m diameter (neutrally buoyant, $\rho_p = 1.05$ g·cm⁻³, $\pm 5\%$ size distribution) were injected into the inlet tubing of the flow cell during the measurements (P/N 10089, TSI Incorporated, Shoreview, MN). A volume of 10 mL suspension of particles (≈ 0.5 mg·L⁻¹ concentration) was injected right before the PIV measurements were made. Seeding density was kept above 8 particles for an imaged area of 32 pixels \times 32 pixels. A 5 μ m pore size filter was mounted to the outflow tube to prevent recirculation and eventual deposition of the injected particles.

2.1.3. Visualization

For typical PIV measurements a laser strobe is used as light source with a cylindrical lens to limit the illuminated region to the

area of interest. To use conventional PIV setup for visualizing the flow in a spacer-filled channel at different heights the laser beam should have been placed perpendicular to the camera, thus allowing illumination of the flow channel at various heights (z direction). The dimension of the flow channel and the presence of the feed spacer limited the possibility of using conventional PIV. For the presented measurements a modified PIV setup was used which allowed capturing the flow pattern at various heights within the spacer-filled channel.

Particles were visualized using an inverted microscope (Axio Imager, Zeiss Microscopy GmbH, Germany) in combination with a high-speed camera (Fastcam SA5, Photron Inc. San Diego, CA) and a 5 \times objective lens with 0.13 numerical aperture (NA). To narrow the depth of field (DOF), a 550 nm filter (BP 550/25, 537–563 nm) was placed in front of the light source, so that a 42–44 μ m focal depth was achieved, Equation (3)

$$DOF = \frac{\lambda \cdot n}{NA^2} \quad (3)$$

where $\lambda = 0.550$ μ m is the light wavelength and $n = 1.33$ is the refractive index of water.

The camera was set to capture 7000 frames per second (fps) with an exposure time of 1/30,000 s, sufficient to eliminate particle motion blur. The obtained image size was 1024 \times 1024 pixels. For each measurement 100 consecutive frames were processed. The angle of view and DOF allowed capturing an area of approximately one feed spacer mesh element (approximately 4 mm \times 4 mm) from the flow cell (Fig. 2). To obtain a complete overview of the flow pattern in the channel, measurements were repeated at different feed spacer mesh elements (x and y direction) and at different positions along the channel height (z direction), for each experimental condition.

2.1.4. Calculation and visualization of velocity fields

The captured video clips were analysed by a commercially

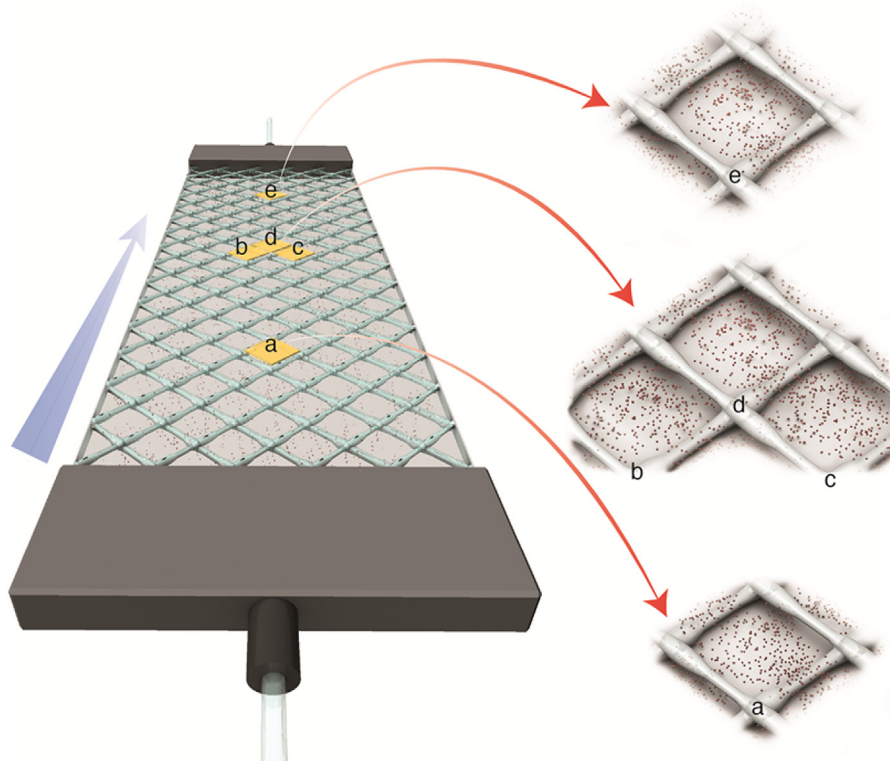


Fig. 2. Schematic representation of the flow cell and the five feed spacer elements (a to e) used to assess the water flow reproducibility at different locations in the flow cell.

available PIV software (DaVis, LaVision GmbH, Goettingen, Germany), using a sequential frame cross correlation method. For quantitative analysis the software was calibrated based on the pixel size ($4 \mu\text{m} \times 4 \mu\text{m}$) on the captured video clips, which was the same for all PIV measurements. The analyses performed on the video data were the calculation of velocity fields and streamlines. The same velocity field calculation procedure was repeated for different z positions (i.e., at maximum 18 different heights in the flow channel). The measured vector fields were visualized and statistically analysed by custom-written routines in MATLAB (MATLAB 2014b, MathWorks, Natick, MA, www.mathworks.com). 100 PIV measurements (i.e., image frames over 0.14 ms (ms)) were taken at each position and averaged in time to minimize the loss of tracked particles.

2.2. Numerical model

Experimental measurements were compared with results from three-dimensional CFD calculations. The model geometry ($4.38 \times 4.38 \times 0.787 \text{ mm}^3$) included one feed spacer mesh element (Fig. 3), with a realistic representation of the spacer geometry constructed with curved surfaces based on Scanning Electron Microscopy images (similar to the procedure from Radu et al., 2014). The hydrodynamic calculations assumed stationary flow of incompressible fluid in laminar flow conditions, according to the Navier–Stokes and continuity Equation (4):

$$\rho(\mathbf{u} \cdot \nabla) \mathbf{u} + \nabla p = \nabla \cdot (\eta \nabla \mathbf{u}),$$

$$\nabla \cdot \mathbf{u} = 0 \quad (4)$$

where $\mathbf{u} = u_x, u_y, u_z$ is the vector of local liquid velocity, p is the pressure, ρ and η are the density and dynamic viscosity of water

(20 °C). Similar to the approach used in Radu et al. (2014), periodic flow conditions were set between the inlet and outlet, as well as between the lateral boundaries (Fig. 3b), implying identical flow velocity fields on pairs of boundaries (in with out and left with right). This approximates the flow profile corresponding to a spacer element situated within an array, sufficiently far from the flow cell walls not to experience entrance/exit or wall effects (Radu et al., 2014). The flow was driven by a pressure difference imposed between inlet and outlet, calculated from an additional constraint such that the desired linear flow velocity u_m is obtained. The water flow was calculated without permeate production, therefore no-slip boundary conditions were set to the top, bottom and spacer surfaces. The steady laminar flow equations were solved in COMSOL Multiphysics (v4.4, Comsol Inc., Burlington, MA) with finite element methods, on a tetrahedral mesh with maximum size of 50 μm .

2.2.1. Calculation and visualization of velocity fields

The flow fields calculated with COMSOL were averaged over intervals of $\Delta z = 40 \mu\text{m}$ before comparing simulation results with the PIV measurements. This averaging procedure was necessary because the measurements were recorded with a depth of field of approx. 40 μm . Therefore, the x – y velocity fields presented at a certain z coordinate should be understood as averages between $z \pm 20 \mu\text{m}$ (Fig. 3a). The flow fields were plotted using a Python script with Matplotlib graphic library (Hunter, 2007), showing streamlines, velocity magnitude and flow direction.

2.2.2. Statistic similarity

The Bray–Curtis similarity was used to analyse the differences between measured and model-calculated 2-D velocity magnitude distributions, as well as the similarity between PIV measurements

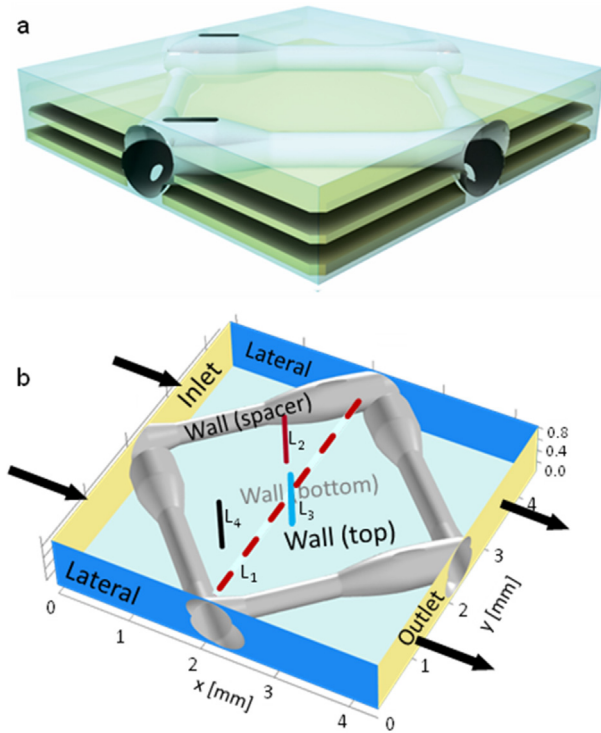


Fig. 3. a) Positions of x – y slices (x coordinate corresponds to the main flow direction and y coordinate is normal to the main flow direction) taken for comparing measured and calculated vector fields at different heights in the flow channel ($z = 200, 400$ and $650 \mu\text{m}$). The three slices have a thickness of $40 \mu\text{m}$ each. b) The computational domain for hydrodynamic simulations includes one spacer element, with spacer resembling the geometry used in practise and positions of cut lines for comparing measured (PIV) and calculated flow velocity as shown in Fig. 9. Line L_1 is in the x – y plane at $x = 2 \text{ mm}$, L_2 – L_4 are in the y – z planes at $(x,y)=(1.48,3.12)$, $(2.06,2.22)$ and $(1.48,1.45) \text{ mm}$, respectively.

at different locations, and between velocity fields averaged over different time intervals. The Bray–Curtis dissimilarity or ‘distance’, d_{BC} , between two sets of data a and b , each containing n points to be compared, is a normalization method defined as (Krebs, 1999):

$$d_{BC} = \frac{\sum_{k=1}^n |a_k - b_k|}{\sum_{k=1}^n (a_k + b_k)} \quad (5)$$

The similarity between the sets a and b was then defined as

$$S_{BC} = 1 - d_{BC} \quad (6)$$

Since all velocity magnitudes are positive, the similarity S_{BC} is always between 0 and 1, with maximum value of 1 for perfectly similar velocity fields.

3. Results

In this study the water flow patterns were investigated in spacer-filled channels using PIV in a flow cell and 3-D CFD techniques under various conditions: (i) varying location along the length and width of the channel, (ii) different measured time frames, and (iii) varying linear flow velocities.

3.1. Flow pattern change over channel height

The PIV measurements allowed the determination of flow velocity patterns in x – y planes, at different heights z in the channel, an example of which is presented in Fig. 4. These planar velocity

fields clearly show how the flow direction changes over the channel height, with two specific zones becoming apparent. Near the bottom (between $z = 0$ and $300 \mu\text{m}$) and near the top walls (between $z = 550$ and $800 \mu\text{m}$) the flow direction mostly follows the nearby located spacer fibre orientation, i.e., at 45° with respect to the main flow direction (Fig. 4). Thus, there is a 90° change in the flow direction from bottom to top, so that in the middle of the channel ($z = 350$ – $500 \mu\text{m}$) a convergence region develops, with the liquid following the main flow direction (left to right in x direction). Because the real spacer geometry includes various positions of filament thinning, the velocity magnitude changes creating zones with fast and slow flow, which are not symmetric against the middle/centre plane at $z = 400 \mu\text{m}$. The maximum measured flow velocity within this experiment was $0.45 \text{ m}\cdot\text{s}^{-1}$ at $z \approx 300 \mu\text{m}$ for the used average flow velocity of $0.163 \text{ m}\cdot\text{s}^{-1}$.

3.2. Spatial reproducibility

To test the method reproducibility and the flow uniformity over the spacer-filled channel, the velocity distribution was measured at five locations (x,y) in the flow cell, as indicated in Fig. 2. The flow patterns were similar at all measured locations, represented in Table 1 at three heights in the channel (Fig. S1, supplementary material). The 2-D flow magnitude distribution at each location was compared by the Bray–Curtis similarity S_{BC} with the average over the five locations. The flow measured at the five locations proved to be very similar, with S_{BC} slightly better for the slices taken near the flow channel bottom and top ($S_{BC} = 0.96$ – 0.98) than for the middle slices ($S_{BC} = 0.94$ – 0.96), indicating that a measurement taken at any spacer cell could be considered representative of the entire flow channel. The rest of the measurements in this study were therefore done in the feed spacer mesh element d , located as shown in Fig. 2.

3.3. Steady and unsteady flow – effect of different flow velocities

In order to study the effect of water velocity on the flow regime, measurements were done at three linear velocities: a reference velocity of $0.163 \text{ m}\cdot\text{s}^{-1}$, which is commonly used in practical operation (Vrouwenvelder et al., 2009), a lower velocity of $0.074 \text{ m}\cdot\text{s}^{-1}$ and a higher velocity of $0.294 \text{ m}\cdot\text{s}^{-1}$. These correspond to Reynolds numbers 160, 70 and 300, respectively. The velocity magnitude for 100 consecutive measurements in time (all at the same point $x = 2 \text{ mm}$, $y = 2 \text{ mm}$) is plotted in Fig. 5 for the three Re numbers. As the Re number increases, larger fluctuations of measured velocity can be observed. At $\text{Re} = 70$ the flow is shown to be stable in time and it can be considered steady. At $\text{Re} = 300$ fluctuations between 20 and 50% of the linear flow velocity were recorded, which clearly indicate an unsteady flow regime. The flow at $\text{Re} = 160$ (as used in practise) shows only a mildly unsteady behaviour with fluctuations of 10% from average velocity. Most flow fluctuations seemed to occur near the top and bottom walls of the spacer-filled flow channel in the regions with the highest local flow velocities.

To quantitatively assess the error associated with time-averaging, the velocity field at $\text{Re} = 160$ was averaged over three time intervals Δt : 0.14 ms (2 frames or 1 measurement), 1.4 ms (10 measurements) and 14 ms (100 measurements), shown in Fig. 6. The Bray–Curtis similarity was then calculated relative to the largest time scale ($\Delta t = 14 \text{ ms}$), showing a 94% similarity for the velocity field averaged over 1.4 ms and 90% similarity for 1 measurement (0.14 ms).

The time averaged measured velocity distributions at three Re at different heights in the channel is presented in Fig. 7. Similar flow regions as for the $\text{Re} = 160$ can also be observed for $\text{Re} = 70$ and

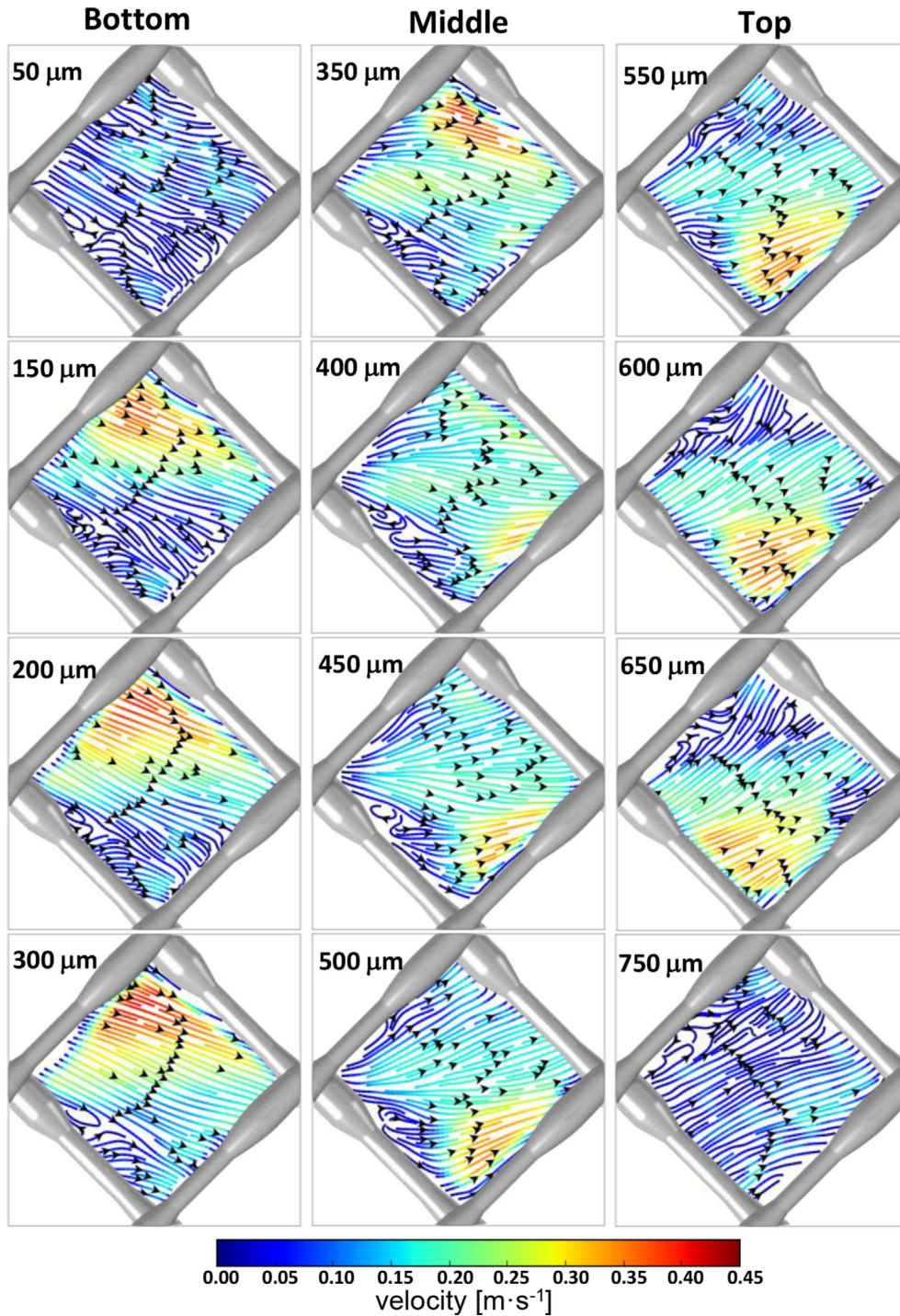


Fig. 4. Measured flow pattern in x - y slices at different heights in the flow channel (z direction, the heights should be interpreted as the middle of the region where the measurements were taken, e.g. $50\ \mu\text{m}$ represents the region between 30 and $70\ \mu\text{m}$ in the channel) showing streamlines and flow direction (black arrows). The flow velocity magnitude is represented by the colour scale of a streamline. The main flow direction with an average flow velocity of $0.163\ \text{m}\cdot\text{s}^{-1}$ ($\text{Re} = 160$) was from left to right. (For interpretation of the references to colour in this figure legend, the reader is referred to the web version of this article.)

300 : high and mostly one-directional velocities near the top and bottom walls and a flow convergence region with slower flow in the middle of the channel, where the flow changes direction. For $\text{Re} = 300$, however, eddies (recirculation zones) were observed in the lower region of the channel (Fig. 7, $z = 200\ \mu\text{m}$, $\text{Re} = 300$). The maximum measured flow velocities were 0.20 , 0.45 and $0.64\ \text{m}\cdot\text{s}^{-1}$ at $\text{Re} = 70$, 160 and 300 , respectively. The nonlinear increase of the measured maximum velocity with the increase of Re indicates a

change in the flow regime from laminar to transitional or turbulent at $\text{Re}300$ (where at a linear increase the maximum velocity would have been 0.82 instead of the observed $0.64\ \text{m}\cdot\text{s}^{-1}$).

3.4. Measurements compared with CFD model

Flow fields determined with PIV at $\text{Re} = 70$, 160 and 300 were compared with those resulted from fluid dynamics calculations,

Table 1

Spatial reproducibility of measured flow field at five locations in the flow cell (a to e), at three different heights in the flow channel $z = 200, 400$ and $650 \mu\text{m}$.

Bray – Curtis similarity (S_{BC})					
Height in the channel	position ^a				
	a	b	c	d	e
$z = 200 \mu\text{m}$	0.97	0.98	0.96	0.98	0.97
$z = 400 \mu\text{m}$	0.95	0.94	0.94	0.96	0.95
$z = 650 \mu\text{m}$	0.96	0.98	0.97	0.98	0.97

^a See Fig. 2.

using steady laminar incompressible Navier–Stokes equations. An example of computed flow represented by streamlines clearly shows the two main flow directions near the top and bottom membrane surfaces (Fig. 8a). Velocity components u_x , u_y and u_z at three heights in the channel are presented in Fig. 8b and Fig. S2 (supplementary material) for a CFD simulation at $Re = 160$. The dominant velocity component is in the x direction (u_x between 0 and $0.4 \text{ m}\cdot\text{s}^{-1}$), whilst the u_y component is more important close to the top and bottom walls, with ranges between -0.3 and $0.3 \text{ m}\cdot\text{s}^{-1}$ and near-zero values in the middle of the channel (at $z = 400 \mu\text{m}$) where the flow changes direction. The vertical velocity component, u_z , has the largest values mostly close to the spacer fibres (between -0.2 and $0.2 \text{ m}\cdot\text{s}^{-1}$), in the regions where the flow passes from one feed spacer mesh element to another.

Comparisons between measured and calculated x – y velocity projections, $\sqrt{u_x^2 + u_y^2}$, in different planes z are presented in Fig. 7. The Bray–Curtis similarity between measured and calculated velocity distributions are good overall ($S_{BC} > 0.84$). It appears that the model predicts better the velocity distributions at lower Re , where the laminar flow was shown to be steady (Fig. 5). However, at $Re = 160$, where slight velocity fluctuations were measured, the model assuming steady laminar flow still compares favourably to the experimental data (Fig. 7). At $Re = 300$, the steady laminar assumption does not hold anymore and the measurements cannot be compared with steady flow calculations. The measured maximum velocity ($0.64 \text{ m}\cdot\text{s}^{-1}$) was $\sim 30\%$ less than the velocity calculated with steady laminar flow ($0.82 \text{ m}\cdot\text{s}^{-1}$).

Measured velocity profiles can also be compared with numerical model results along cut lines in the z direction, as shown in Fig. 3b. This comparison between measured and modelled flow data along a 1-D profile enables further (and more direct) evaluation of model accuracy. For example, calculated velocities on a line across the

main flow direction in the middle of a feed spacer mesh element, shown in Fig. 9a, exhibit good agreement with the measurements. Several steps and maxima can be observed in the measured velocity profiles near the bottom ($z = 200 \mu\text{m}$) and top ($z = 650 \mu\text{m}$) walls, which are also revealed by the simulations. Also, the velocity magnitude is correctly calculated, with a steep change from $0 \text{ m}\cdot\text{s}^{-1}$ next to the spacer to a maximum of $0.4 \text{ m}\cdot\text{s}^{-1}$ on the opposite side. In the middle section ($z = 400 \mu\text{m}$) the velocity changes within a narrower interval, showing 3–4 peaks. The discrepancies in terms of local velocity peaks between the simulations and the experimental measurements can most likely be attributed to the simplified spacer geometry adopted in the model (the model geometry was constructed with parametric surfaces to approximate the SEM measurements). Measurements of the x – y projected velocities at different heights z in the channel, shown in Fig. 9b, are more difficult to perform and with less resolution. Along line L_3 in the middle of the feed spacer mesh element two velocity peaks can be observed on the measured and calculated velocity profiles.

4. Discussion

In this study water flow in a spacer-filled channel under hydrodynamic conditions used in practice was evaluated. PIV measurements at different locations along the spacer-filled channel of the flow cell at varying heights revealed steady and laminar flow conditions at linear flow velocities commonly used in practice ($u_m = 0.05$ – $0.2 \text{ m}\cdot\text{s}^{-1}$), where also the 3-D CFD simulations were in good agreement with the measured data.

4.1. Flow regimes

An important result of this study is that the possibility of laminar and steady flow in the velocity range used in practice ($u_m = 0.07$ – $0.2 \text{ m}\cdot\text{s}^{-1}$) was confirmed. The flow appears to be laminar with only slight unsteadiness in the upper velocity limit. Although a velocity of $0.2 \text{ m}\cdot\text{s}^{-1}$ can be achieved in the lead module of a membrane plant, as permeate is produced along the modules, the velocity drops towards the end and it can reach $0.07 \text{ m}\cdot\text{s}^{-1}$ (Malek et al., 1996). Higher velocities, where the flow was observed to be unsteady (e.g. $0.3 \text{ m}\cdot\text{s}^{-1}$), are not commonly used in practice for spiral wound reverse osmosis or nanofiltration modules, as these would result in large axial pressure drops. However, the presence of laminar flow in our experimental conditions should be cautiously interpreted, because in these flow-cell measurements a

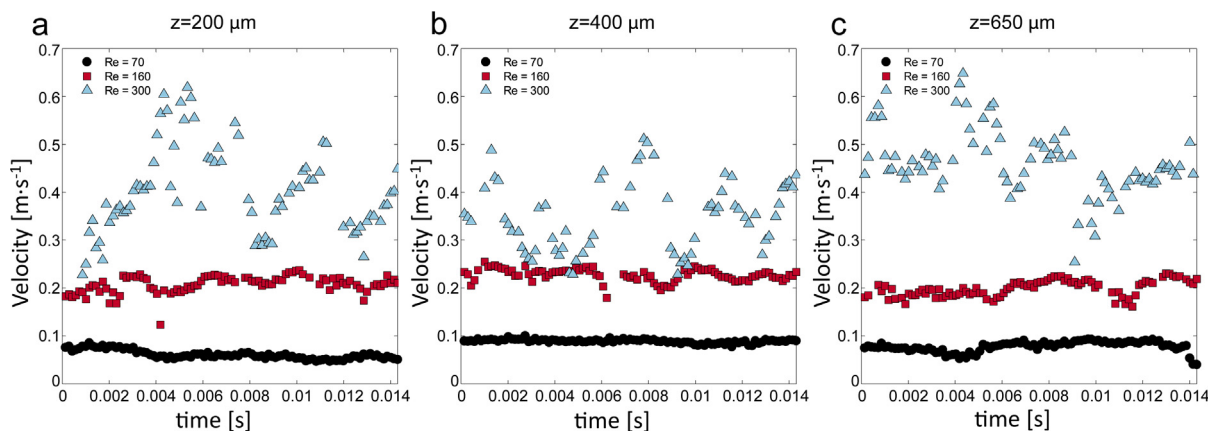


Fig. 5. Measured local velocity magnitude over time at three flow velocities (corresponding to $Re = 70, 160$ and 300), in the middle of a feed spacer element ($x = 2 \text{ mm}, y = 2 \text{ mm}$) at different heights in the flow channel: a) $z = 200 \mu\text{m}$, b) $z = 400 \mu\text{m}$ and c) $z = 650 \mu\text{m}$. While the flow is mostly steady at $Re = 70$, it changes to unsteady (large velocity fluctuations) at $Re = 300$. The flow at $Re = 160$ is only slightly unsteady.

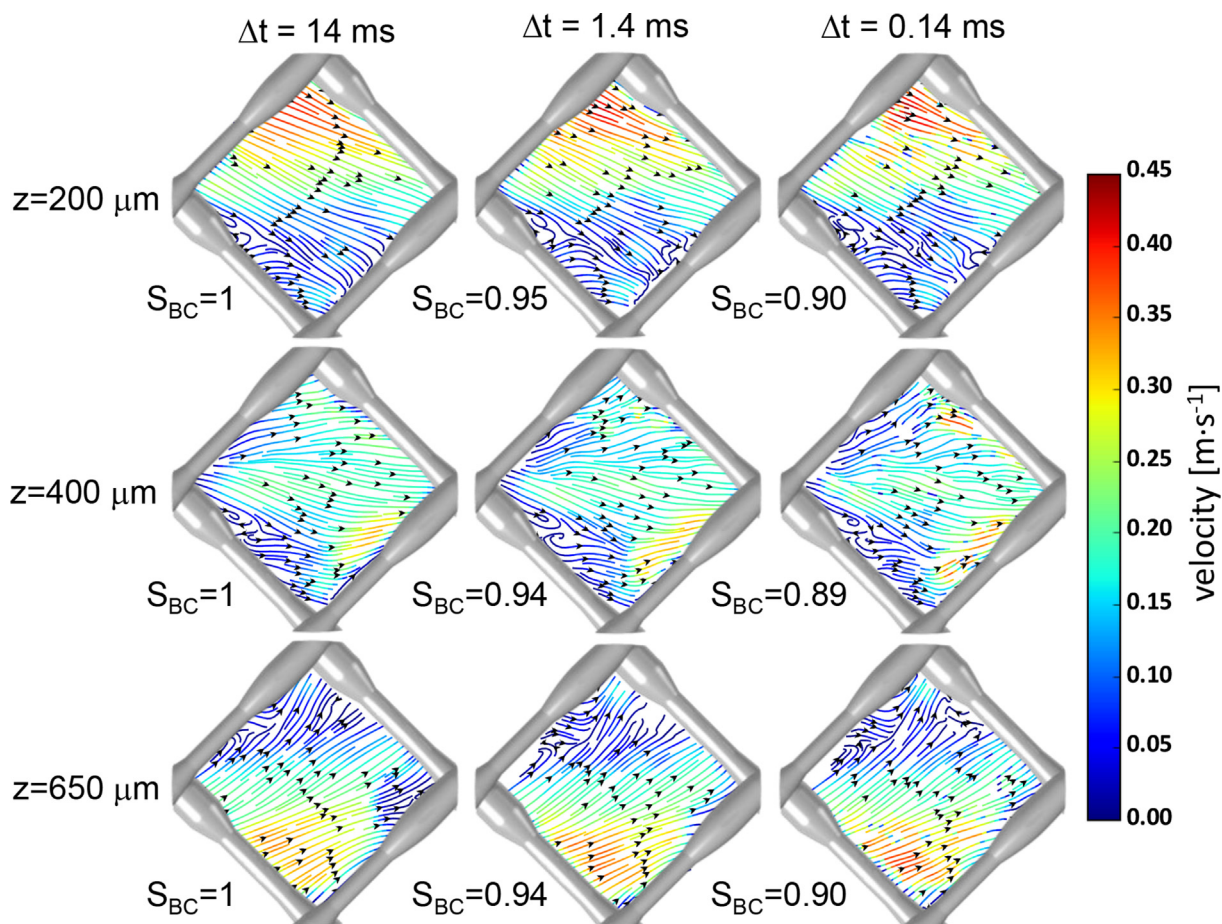


Fig. 6. Time-dependence of the measured flow field at different heights in the channel $z = 200, 400$ and $650 \mu\text{m}$. 2-D distributions of the flow velocity are shown averaged over periods of 0.14 ms , 1.4 ms and 14 ms . The Bray–Curtis similarity (S_{BC}) was calculated relative to the largest imaging time scale ($\Delta t = 14 \text{ ms}$). The main flow direction with an average flow velocity of $0.163 \text{ m}\cdot\text{s}^{-1}$ ($Re = 160$) was from left to right. Streamlines and colour scale are as in Fig. 4. (For interpretation of the references to colour in this figure legend, the reader is referred to the web version of this article.)

constant inlet velocity was achieved. It is still possible that in practice the unsteady flow starts to develop at lower velocities if the inlet flow rate is not very well controlled and fluctuates.

A previous study on PIV measurements for Re up to 4000 (Gimmelshtein and Semiat, 2005) reported laminar flow up to $Re = 1200$ with small fluctuations using feed spacer with a thickness of $800 \mu\text{m}$ ($\approx 31 \text{ mil}$). These results are in contrast with the findings of the current study, where for $Re > 200$ unsteady transient flow was measured. However, one should note that the equation used to calculate Re in Gimmelshtein and Semiat (2005) was based on the channel height and did not include any correction to account for the spacer presence.

$$Re = \frac{2 \cdot u \cdot h \cdot \rho}{\eta} \quad (7)$$

where u is the magnitude of local liquid velocity, ρ and η are the density and dynamic viscosity of water and h is the channel height.

Based on the equation used in Gimmelshtein and Semiat (2005), the Re at linear flow velocities used in this study are 110, 256 and 463. Mojab et al. (2010) evaluated experimentally and with a numerical model flow characteristics for a spacer geometry scaled-up by a factor 10 compared to the commonly used spacer thickness for Re ranging from 100 to 1000 and reported that transition from steady to unsteady flow occurred above $Re = 250$.

Flow field measurements using Doppler OCT indicated the

presence of swirling flows next to the spacer filaments in the vertical (y – z) plane at a linear flow velocity of $0.03 \text{ m}\cdot\text{s}^{-1}$ (Gao et al., 2013). It was expected to capture the impact of the swirling flows (in the y – z plane) on the flow captured with PIV in x – y planes, taking in consideration that the Doppler OCT measurements were performed at a much lower linear flow velocity than the PIV measurements, however, no eddies or disturbed flow were found until an inflow velocity of $\sim 0.3 \text{ m}\cdot\text{s}^{-1}$. These differences might point to the need for an improved interpretation of Doppler OCT images, as also suggested by Gao et al. (2013).

The water flow velocities over the spacer-filled channel height were measured in this study with a much higher spatial resolution ($\Delta z = 40 \mu\text{m}$, Figs. 4 and 9b) than in a previous report of spacer-filled channels for membrane filtration processes ($\Delta z = 300$ – $600 \mu\text{m}$ in Willems et al., 2010). This allowed capturing the gradual change in flow direction over the flow channel height (z direction). Focussing on only one feed spacer mesh element provided a more accurate x – y resolution than in other studies, revealing more details of the flow structure and the existence of small recirculation zones behind the spacers at $Re = 160$ (Fig. 4), and even larger recirculation zones at $Re = 300$ (Fig. 7).

Repeated measurements in different feed spacer mesh elements along the flow cell showed that the flow pattern is very similar at all monitored locations. Similar results were obtained in particle deposition experiments (Radu et al., 2014). This indicates that flow observations performed in small flow cells are representative, at

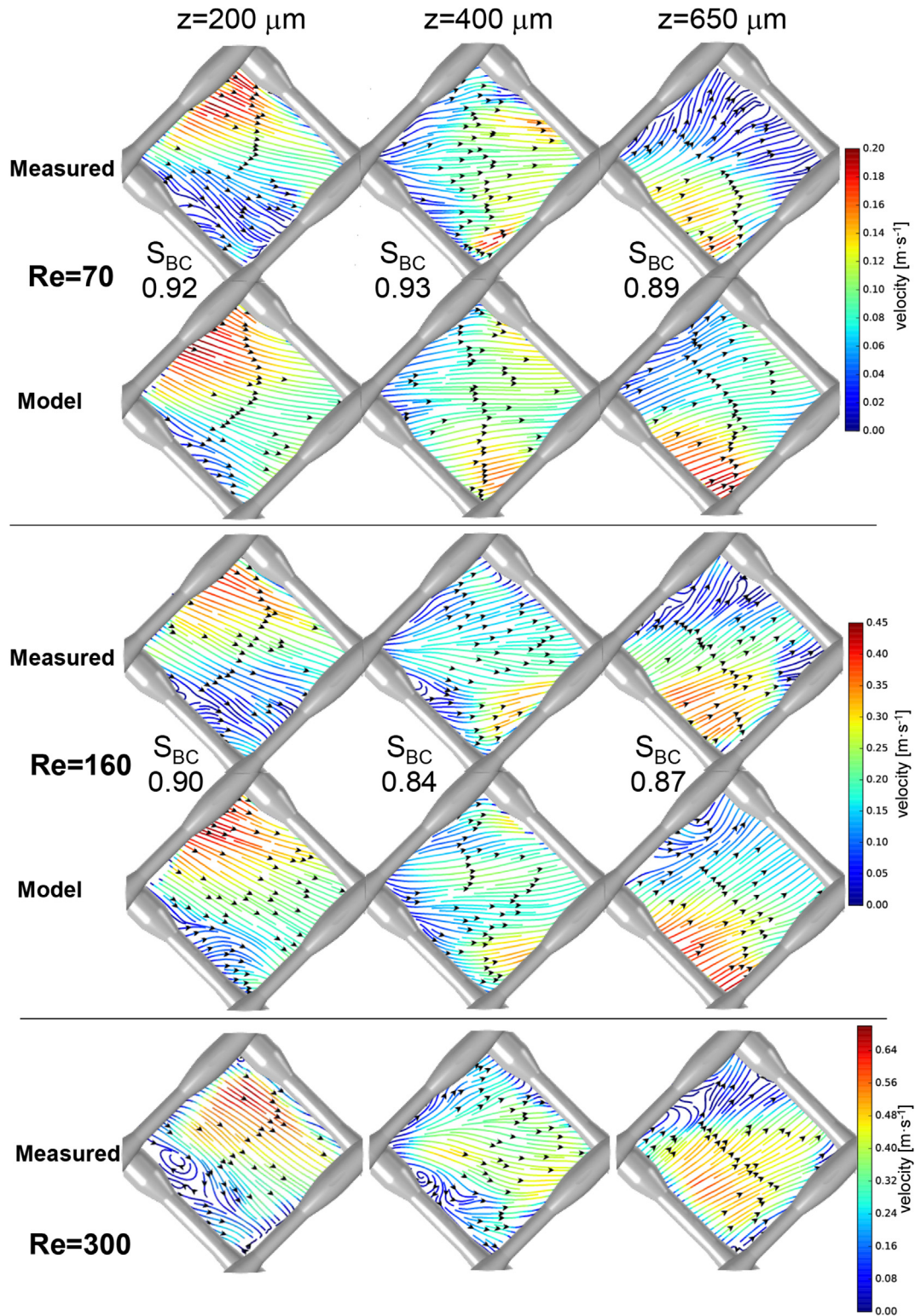


Fig. 7. Comparison between measured and calculated flow fields at $Re = 70$ (top), $Re = 160$ (middle) and $Re = 300$ (bottom), at three channel heights $z = 200, 400$ and $650 \mu\text{m}$. Streamlines show as colour scale the flow velocity magnitude. S_{BC} numbers represent the calculated similarity indices (Bray–Curtis) between measured and calculated 2-D velocity distributions. (For interpretation of the references to colour in this figure legend, the reader is referred to the web version of this article.)

least for clean (i.e., not fouled) modules.

4.2. Solute transfer

Understanding the detailed (micro-scale) flow dynamics is

relevant for understanding solute transport (e.g., salts) and for the design of feed spacers that promote the best mixing possible with the least energy input. Our results clearly demonstrate the existence of faster flow near the top and bottom membrane surfaces and a slower flow in the middle of the flow channel. The fast flow

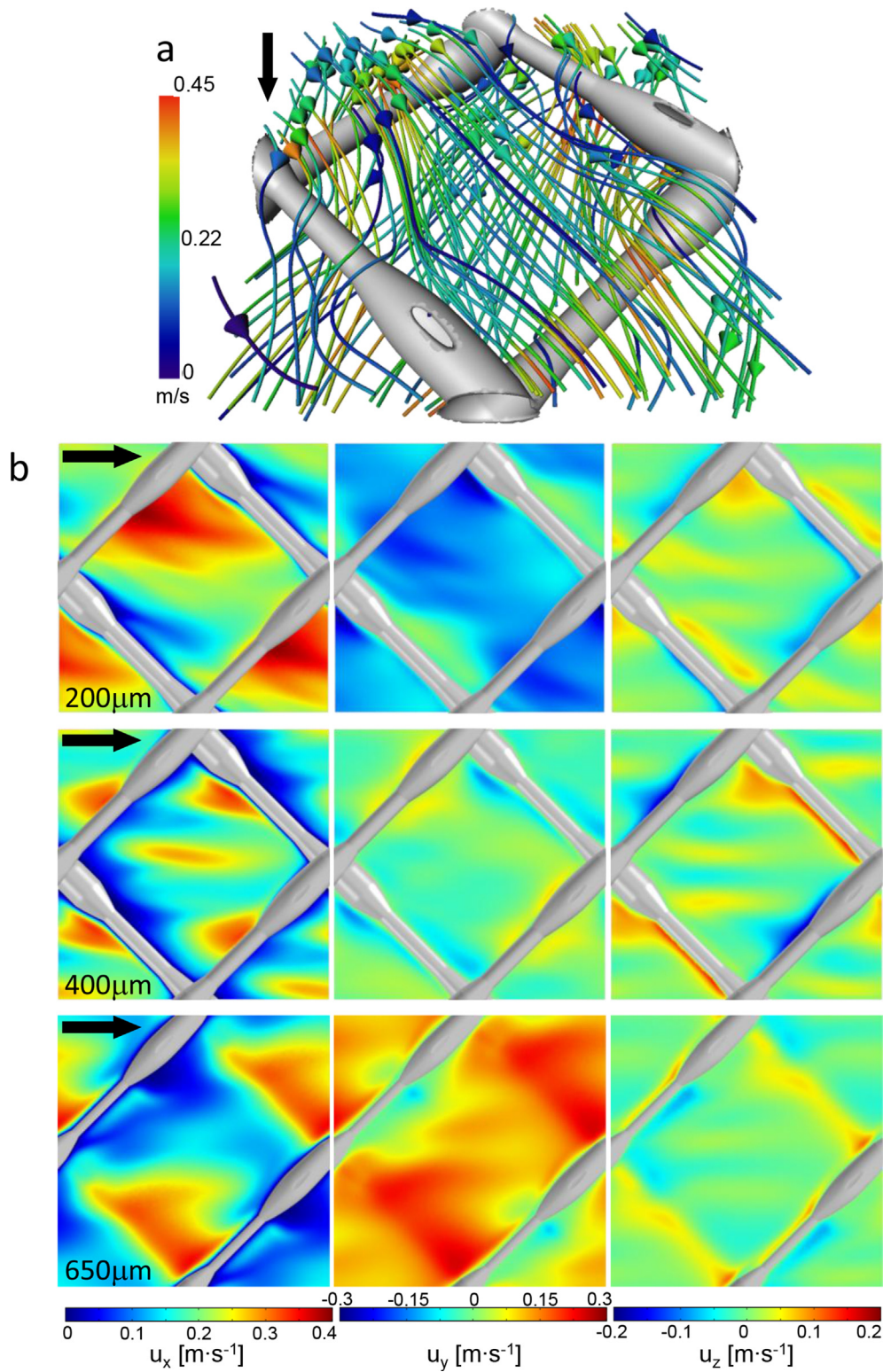


Fig. 8. (a) Streamlines of simulated flow in a feed spacer element (flow direction from top to bottom). Colours show the velocity magnitude from $0 \text{ m}\cdot\text{s}^{-1}$ (blue) to $0.45 \text{ m}\cdot\text{s}^{-1}$ (orange). (b) Computed distribution of velocity components u_x , u_y and u_z at two heights in the flow channel (200, 400 and $650 \mu\text{m}$). The CFD simulation was made at $\text{Re} = 160$, assuming steady laminar flow (direction from left to right). (For interpretation of the references to colour in this figure legend, the reader is referred to the web version of this article.)

will result in better solute transfer near the membranes, where the concentration polarization layer forms. However, the existence of recirculation zones at the linear velocities used in practice seems to

be limited. Moreover, the slow laminar flow in the last module (at the end of the pressure vessel with the lowest velocity) would favour salt precipitation and scaling. Knowledge of the detailed

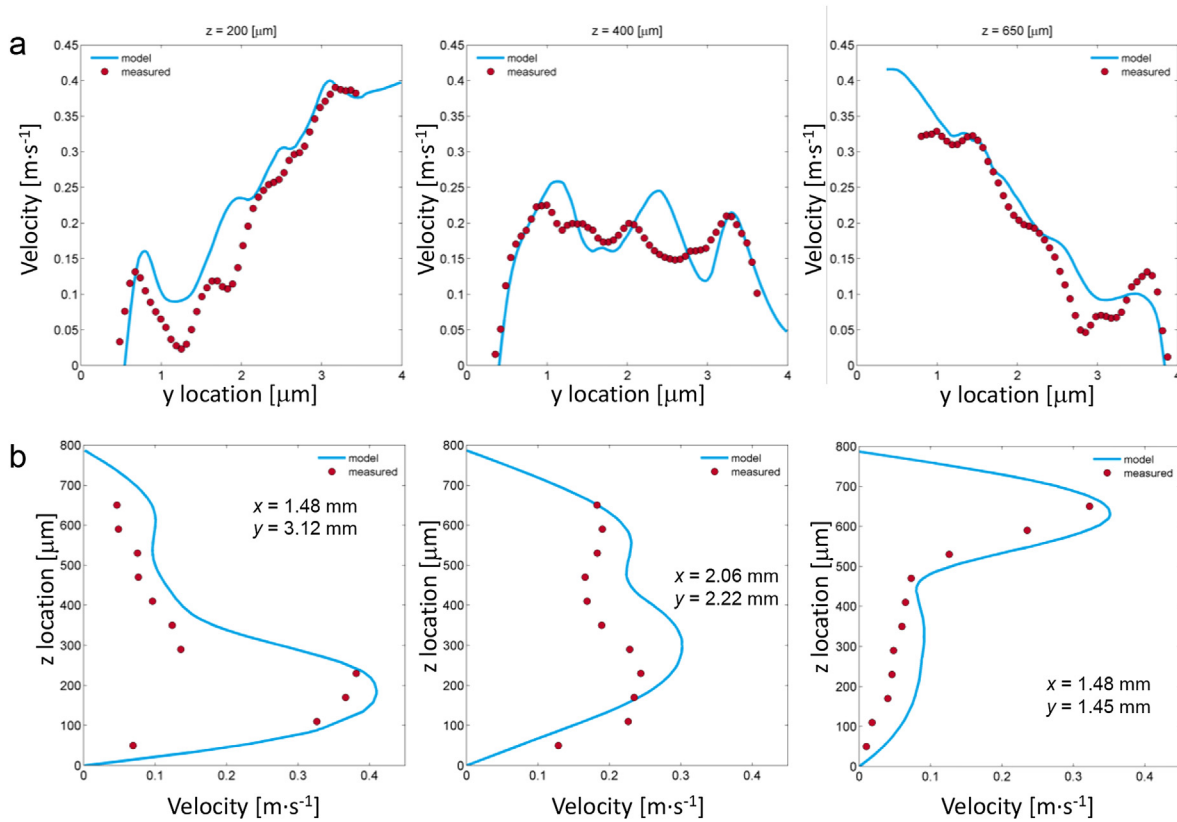


Fig. 9. Comparison between measured (circle symbols) and calculated (lines) flow velocity magnitude along a line perpendicular to the main flow direction (a) line L_1 in the x - y plane at $x \approx 2$ mm and different channel heights ($z = 200, 400$ and $650 \mu\text{m}$), and (b) lines L_2, L_3, L_4 in the y - z plane at different x and y positions (see Fig. 3 for positions of L_1 - L_4). The CFD simulation was made at $Re = 160$, assuming steady laminar flow.

flow features could allow further investigations of mass transfer coefficients in the feed channel, using the constant wall concentration approach as suggested in Koutsou et al. (2009) and Fimbres-Weihs and Wiley (2010).

4.3. CFD model

A key result of this study is the good agreement between the PIV measured and the computed water flow fields. It reveals that the steady laminar flow assumption in the CFD simulations allows a good description of the actual flow in the spacer-filled channel. Furthermore, the obtained results also imply that for clean flow channels the computational domain can be reduced to one feed spacer mesh element with periodic boundary conditions for hydrodynamic calculations, if permeation flux contribution to velocity change is negligible. This approach gives confidence in pursuing model-based studies for designing other feed spacer geometries with reduced pressure drop and fouling, while still providing good solute transfer. Flow pattern has been shown (Radu et al., 2014) to be of crucial importance in the deposition and development of foulant layers, both for scaling and for biofouling.

The velocity field resulted from numerical simulations is sensitive to the accuracy (or realism) of used feed spacer geometry, which influences the comparison with experimental measurements. It is therefore imperative that the 3-D spacer geometry is represented in the model as closely as possible to the real shape of spacers used in practice. This has been pointed out also by other numerical and experimental studies (Picioreanu et al., 2009; Radu et al., 2014). In future studies we will use directly the solid geometries reconstructed from computerized tomography (CT) scans.

4.4. Further studies

The focal depth on the channel height (z) was set here with approximation within $40 \mu\text{m}$. A narrower focal depth would allow taking more optical slices, thus more resolution over the channel height. For this, other lenses with higher numerical aperture and other light sources with lower wavelength (e.g., UV light) could be used.

Tomographic PIV would allow for capture of the flow velocity component in the z -direction (Elsinga et al., 2006; Casey et al., 2013). However, for such a narrow flow channel it would be very difficult to set up cameras to measure the flow from a lateral view. Especially, the presence of an opaque feed spacer will not allow the lateral observation of the flow channel.

For further model validation, other spacer geometries and spacer orientation should be tested. It is of interest to evaluate the impact of fouling on the local velocity field, since the water flow may become unsteady at lower linear flow velocities in the presence of fouling. It should also be tested whether the methods could be applied for forward osmosis (FO) and pressure-retarded osmosis (PRO) flow channels.

5. Conclusions

A particle image velocimetry (PIV) method was implemented to measure detailed water flow fields in a flow-cell simulating at small scale conditions encountered in the feed spacer-filled flow channels of spiral-wound membrane modules. Narrow focal depth allowed optical sectioning at multiple (maximum 18) levels along the channel height of this lab-scale spacer-filled flow channel.

At linear velocities between $u = 0.07\text{--}0.2 \text{ m}\cdot\text{s}^{-1}$ (as used in practice) the measured flow appears to be laminar with only slight unsteadiness in the upper velocity limit. At higher velocities ($0.3 \text{ m}\cdot\text{s}^{-1}$) the flow was observed to be unsteady with appearance of local recirculation zones.

Measurements taken at different locations in the flow cell (in several feed spacer mesh elements) showed very similar water flow patterns ($S_{BC} = 0.94\text{--}0.98$), indicating the same hydrodynamic conditions along and across a small flow channel without permeate production.

Computational fluid dynamics simulations based on steady laminar flow assumption were in good agreement with the measured flow fields (lowest $S_{BC} = 0.84$). This supports the use of model-based studies in the optimization of spacer geometries and operational conditions.

Acknowledgements

The research reported in this paper was supported by King Abdullah University of Science and Technology. The authors gracefully acknowledge Ivan Gromicho, Heno Hwang, for assistance with the illustrations and Galina Printsypar and Thomas Theussl for their support in the statistical analyses and data visualization from King Abdullah University of Science and Technology.

Appendix A. Supplementary data

Supplementary data related to this article can be found at <http://dx.doi.org/10.1016/j.watres.2015.09.036>.

References

- Antony, A., Low, J.H., Gray, S., Childress, A.E., Le-Clech, P., Leslie, G., 2011. Scale formation and control in high pressure membrane water treatment systems: a review. *J. Memb. Sci.* 383, 1–16. <http://dx.doi.org/10.1016/j.memsci.2011.08.054>.
- Araújo, P.A., Kruihof, J.C., Van Loosdrecht, M.C.M., Vrouwenvelder, J.S., 2012. The potential of standard and modified feed spacers for biofouling control. *J. Memb. Sci.* 403–404, 58–70. <http://dx.doi.org/10.1016/j.memsci.2012.02.015>.
- Baker, J.S., Dudley, L.Y., 1998. Biofouling in membrane systems — A review. *Desalination* 118, 81–89. [http://dx.doi.org/10.1016/S0011-9164\(98\)00091-5](http://dx.doi.org/10.1016/S0011-9164(98)00091-5).
- Bucs, S.S., Radu, A.I., Lavric, V., Vrouwenvelder, J.S., Picioreanu, C., 2014. Effect of different commercial feed spacers on biofouling of reverse osmosis membrane systems: a numerical study. *Desalination* 343, 26–37. <http://dx.doi.org/10.1016/j.desal.2013.11.007>.
- Casey, T.A., Sakakibara, J., Thoroddsen, S.T., 2013. Scanning tomographic particle image velocimetry applied to a turbulent jet. *Phys. Fluids* 25, 025102. <http://dx.doi.org/10.1063/1.4790640>.
- Elsinga, G.E., Scarano, F., Wieneke, B., Oudheusden van, B.W., 2006. Tomographic particle image velocimetry. *Exp. Fluids* 41, 933–947.
- Fimbres-Weihs, G.A., Wiley, D.E., 2010. Review of 3D CFD modeling of flow and mass transfer in narrow spacer-filled channels in membrane modules. *Chem. Eng. Process. Process Intensif.* 49, 759–781. <http://dx.doi.org/10.1016/j.cep.2010.01.007>.
- Fimbres-Weihs, G.A., Wiley, D.E., Fletcher, D.F., 2006. Unsteady flows with mass transfer in narrow zigzag spacer-filled channels: a numerical study. *Ind. Eng. Chem. Res.* 45, 6594–6603. <http://dx.doi.org/10.1021/ie060243l>.
- Flemming, H.-C., 2002. Biofouling in water systems—cases, causes and countermeasures. *Appl. Microbiol. Biotechnol.* 59, 629–640. <http://dx.doi.org/10.1007/s00253-002-1066-9>.
- Flemming, H.-C., 1997. Reverse osmosis membrane biofouling. *Exp. Therm. Fluid Sci.* 14, 382–391. [http://dx.doi.org/10.1016/S0894-1777\(96\)00140-9](http://dx.doi.org/10.1016/S0894-1777(96)00140-9).
- Gao, Y., Haavisto, S., Tang, C.Y., Salmela, J., Li, W., 2013. Characterization of fluid dynamics in spacer-filled channels for membrane filtration using Doppler optical coherence tomography. *J. Memb. Sci.* 448, 198–208. <http://dx.doi.org/10.1016/j.memsci.2013.08.011>.
- Gimmelshtein, M., Semiat, R., 2005. Investigation of flow next to membrane walls. *J. Memb. Sci.* 264, 137–150. <http://dx.doi.org/10.1016/j.memsci.2005.04.033>.
- Hunter, J.D., 2007. *Matplotlib: A 2D graphics environment*. *Comput. Sci. Eng.* 9, 90–95.
- Ishigami, T., Amano, K., Fujii, A., Ohmukai, Y., Kamio, E., Maruyama, T., Matsuyama, H., 2012. Fouling reduction of reverse osmosis membrane by surface modification via layer-by-layer assembly. *Sep. Purif. Technol.* 99, 1–7. <http://dx.doi.org/10.1016/j.seppur.2012.08.002>.
- Koutsou, C.P., Yiantsios, S.G., Karabelas, A.J., 2009. A numerical and experimental study of mass transfer in spacer-filled channels: effects of spacer geometrical characteristics and Schmidt number. *J. Memb. Sci.* 326, 234–251. <http://dx.doi.org/10.1016/j.memsci.2008.10.007>.
- Koutsou, C.P., Yiantsios, S.G., Karabelas, A.J., 2007. Direct numerical simulation of flow in spacer-filled channels: effect of spacer geometrical characteristics. *J. Memb. Sci.* 291, 53–69. <http://dx.doi.org/10.1016/j.memsci.2006.12.032>.
- Krebs, C.J., 1999. *Ecological Methodology*, second ed. (Benjamin/Cummings).
- Liu, J., Liu, Z., Xu, X., Liu, F., 2015. Saw-tooth spacer for membrane filtration: hydrodynamic investigation by PIV and filtration experiment validation. *Chem. Eng. Process. Process Intensif.* 91, 23–34. <http://dx.doi.org/10.1016/j.cep.2015.03.013>.
- Malek, A., Hawlader, M.N.A., Ho, J.C., 1996. Design and economics of RO seawater desalination. *Desalination* 105, 245–261. [http://dx.doi.org/10.1016/0011-9164\(96\)00081-1](http://dx.doi.org/10.1016/0011-9164(96)00081-1).
- Manz, B., Volke, F., Goll, D., Horn, H., 2003. Measuring local flow velocities and biofilm structure in biofilm systems with magnetic resonance imaging (MRI). *Biotechnol. Bioeng.* 84, 424–432. <http://dx.doi.org/10.1002/bit.10782>.
- Mojab, S.M., Hanff, E.S., Beale, S.B., Pollard, A., Pharoah, J.G., 2010. Particle image velocimetry investigation of flows within spacer-filled channels. In: *15th Int Symp on Applications of Laser Techniques to Fluid Mechanics*. Lisbon.
- Picioreanu, C., Vrouwenvelder, J.S., van Loosdrecht, M.C.M., 2009. Three-dimensional modeling of biofouling and fluid dynamics in feed spacer channels of membrane devices. *J. Memb. Sci.* 345, 340–354. <http://dx.doi.org/10.1016/j.memsci.2009.09.024>.
- Radu, A.I., van Steen, M.S.H., Vrouwenvelder, J.S., van Loosdrecht, M.C.M., Picioreanu, C., 2014. Spacer geometry and particle deposition in spiral wound membrane feed channels. *Water Res.* 64, 160–176. <http://dx.doi.org/10.1016/j.watres.2014.06.040>.
- Radu, A.I., Vrouwenvelder, J.S., van Loosdrecht, M.C.M., Picioreanu, C., 2010. Modeling the effect of biofilm formation on reverse osmosis performance: flux, feed channel pressure drop and solute passage. *J. Memb. Sci.* 365, 1–15. <http://dx.doi.org/10.1016/j.memsci.2010.07.036>.
- Ridgway, H.F., Kelly, A., Justice, C., Olson, B.H., 1983. Microbial fouling of reverse-osmosis membranes used in advanced wastewater treatment technology: chemical, bacteriological, and ultrastructural analyses. *Appl. Environ. Microbiol.* 45, 1066–1084.
- Sablani, S., Goosen, M.F., Al-Belushi, R., Wilf, M., 2001. Concentration polarization in ultrafiltration and reverse osmosis: a critical review. *Desalination* 141, 269–289. [http://dx.doi.org/10.1016/S0011-9164\(01\)85005-0](http://dx.doi.org/10.1016/S0011-9164(01)85005-0).
- Saeed, A., Vuthaluru, R., Yang, Y., Vuthaluru, H.B., 2012. Effect of feed spacer arrangement on flow dynamics through spacer filled membranes. *Desalination* 285, 163–169. <http://dx.doi.org/10.1016/j.desal.2011.09.050>.
- Salvador Cob, S., Beaupin, C., Hof, B., Nederlof, M.M., Harmsen, D.J.H., Cornelissen, E.R., Zwijnenburg, A., Genceli Güner, F.E., Witkamp, G.J., 2012. Silica and silicate precipitation as limiting factors in high-recovery reverse osmosis operations. *J. Memb. Sci.* 423–424, 1–10. <http://dx.doi.org/10.1016/j.memsci.2012.07.016>.
- Schock, G., Miquel, A., 1987. Mass transfer and pressure loss in spiral wound modules. *Desalination* 64, 339–352. [http://dx.doi.org/10.1016/0011-9164\(87\)90107-X](http://dx.doi.org/10.1016/0011-9164(87)90107-X).
- Schwinge, J., Wiley, D.E., Fletcher, D.F., 2002. Simulation of the flow around spacer filaments between channel walls. 2. mass-transfer enhancement. *Ind. Eng. Chem. Res.* 41, 4879–4888. <http://dx.doi.org/10.1021/ie011015o>.
- Tang, C.Y., Chong, T.H., Fane, A.G., 2011. Colloidal interactions and fouling of NF and RO membranes: a review. *Adv. Colloid Interface Sci.* 164, 126–143. <http://dx.doi.org/10.1016/j.cis.2010.10.007>.
- Valladares Linares, R., Bucs, S.S., Li, Z., AbuGhdeeb, M., Amy, G., Vrouwenvelder, J.S., 2014. Impact of spacer thickness on biofouling in forward osmosis. *Water Res.* 57, 223–233. <http://dx.doi.org/10.1016/j.watres.2014.03.046>.
- Vrouwenvelder, J.S., Graf von der Schulenburg, D.A., Kruihof, J.C., Johns, M.L., van Loosdrecht, M.C.M., 2009a. Biofouling of spiral-wound nanofiltration and reverse osmosis membranes: a feed spacer problem. *Water Res.* 43, 583–594. <http://dx.doi.org/10.1016/j.watres.2008.11.019>.
- Vrouwenvelder, J.S., Picioreanu, C., Kruihof, J.C., van Loosdrecht, M.C.M., 2010. Biofouling in spiral wound membrane systems: three-dimensional CFD model based evaluation of experimental data. *J. Memb. Sci.* 346, 71–85. <http://dx.doi.org/10.1016/j.memsci.2009.09.025>.
- Vrouwenvelder, J.S., van Loosdrecht, M.C.M., Kruihof, J.C., 2011. Early warning of biofouling in spiral wound nanofiltration and reverse osmosis membranes. *Desalination* 265, 206–212. <http://dx.doi.org/10.1016/j.desal.2010.07.053>.
- Vrouwenvelder, J.S., van Paassen, J.A.M., van Agtmaal, J.M.C., van Loosdrecht, M.C.M., Kruihof, J.C., 2009b. A critical flux to avoid biofouling of spiral wound nanofiltration and reverse osmosis membranes: fact or fiction? *J. Memb. Sci.* 326, 36–44. <http://dx.doi.org/10.1016/j.memsci.2008.09.029>.
- Wagner, M., Manz, B., Volke, F., Neu, T.R., Horn, H., 2010. Online assessment of biofilm development, sloughing and forced detachment in tube reactor by means of magnetic resonance microscopy. *Biotechnol. Bioeng.* 107, 172–181. <http://dx.doi.org/10.1002/bit.22784>.
- Willems, P., Deen, N.G., Kemperman, A.J.B., Lammertink, R.G.H., Wessling, M., van Sint Annaland, M., Kuipers, J.A.M., van der Meer, W.G.J., 2010. Use of particle imaging velocimetry to measure liquid velocity profiles in liquid and liquid/gas flows through spacer filled channels. *J. Memb. Sci.* 362, 143–153. <http://dx.doi.org/10.1016/j.memsci.2010.06.029>.
- Yiantsios, S.G., Karabelas, A.J., 2003. Deposition of micron-sized particles on flat surfaces: effects of hydrodynamic and physicochemical conditions on particle attachment efficiency. *Chem. Eng. Sci.* 58, 3105–3113. [http://dx.doi.org/10.1016/S0009-2509\(03\)00169-6](http://dx.doi.org/10.1016/S0009-2509(03)00169-6).